Distortion of the stellar sky by a Schwarzschild black hole

Thomas Müller[a)] and Daniel Weiskopf

Visualisierungsinstitut der Universität Stuttgart (VISUS), Nobelstrasse 15, 70569 Stuttgart, Germany

The optical appearance of the stellar sky for an observer in the vicinity of a black hole is dominated by bending of light, the frequency shift, and the magnification caused by gravitational lensing and aberration. Due to the finite aperture of an observer's eye or a telescope, Fraunhofer diffraction has to be taken into account. We have used high performance graphics hardware and developed a program that enables the user to interactively explore the stellar sky in the vicinity of a Schwarzschild black hole. To do so, we determine what an observer, who can either move quasistatically around the black hole or follow a timelike radial geodesic, would actually see. © *2010 American Association of Physics Teachers.*
[DOI: 10.1119/1.3258282]

I. INTRODUCTION

The Schwarzschild spacetime[1] is the best studied, nontrivial solution of Einstein's equations of the general theory of relativity[2] and is able to describe black holes, one of the most fascinating objects in the universe. The literature[3–5] contains detailed discussions of effects caused by the curved spacetime of the Schwarzschild metric. However, even the best textbooks have limited explanations of relativistic visual effects because books can show only a few fixed situations. Interactive visualizations can play an important role in bridging the gap between mathematical descriptions, theoretical models, and exemplary applications.

The aim of our article is twofold. We discuss the relativistic aspects that influence the first-person view of the stellar sky in the neighborhood of a Schwarzschild black hole. The first-person view is the image that would be recorded by a camera close to the black hole. Our main interest is in the lensing effect. We also discuss the technical details for the interactive point-based visualization of stars in this relativistic context. To be as realistic as possible, we approximate stellar spectra by Planck spectra and also incorporate Fraunhofer diffraction on circular lenses. We have implemented the resulting first-person view in our interactive application, where the user can take the role of an observer who can either move quasistatically around the black hole or fall freely into the singularity.

The most straightforward way to obtain a first-person view of the effects in the neighborhood of a Schwarzschild black hole is four-dimensional ray tracing.[6,7] In brief, the ray tracing method works as follows. A light ray is traced from the observer to the scenery and back in time until it intersects with an object, leaves the region of interest, or is interrupted by a break condition, which means that the light ray leaves the valid spacetime domain or the numerical integration becomes unreliable. All of these criteria must be checked for every single light ray and all its line segments. Hence, the ray tracing method needs a lot of computer resources and is time consuming when many images are needed to generate a movie. However, an interactive visualization becomes possible using programmable graphical processing units (GPUs) and their highly efficient hardware architecture. The aim is to find directly all the light rays connecting the observer to the objects. For that, we have to solve the null geodesic equation as a boundary value problem, which is nearly impossible for an arbitrary four-dimensional spacetime. However, for the Schwarzschild[8] as well as the Morris–Thorne[9] metrics there exist analytical solutions to the null geodesic equation that help solve this boundary value problem.

A detailed discussion of the optical appearance of distant objects to observers near and inside a Schwarzschild black hole was given by Cunningham.[10] Schastok *et al.*[11] illustrated the stellar sky for an observer located at the north pole of the Earth, while increasing its mass until its Schwarzschild radius becomes comparable with its geometrical radius. Nemiroff[12] produced computer generated movies showing the distortion effects near a neutron star and a black hole. The geometric effects observable when falling into a Schwarzschild black hole are discussed by Müller.[13] Readers who wish to become familiar with the nonrelativistic view of the stellar sky can use, for example, the open source programs STELLARIUM[14] or the space simulation CELESTIA.[15] To study the behavior of single null geodesics in the Schwarzschild spacetime, there is a JAVA application by Tuleja[16] or the GEODESICVIEWER by Müller.[17]

Although we focus on the educational aspects of general relativity, effects such as gravitational lensing have found serious interest in astronomy as a tool for studying very distant objects. There are many papers that discuss these effects in detail, and we can give only a few references.[18–24] Because the resolution of telescopes is continually improving, the close neighborhood of our galactic black hole and its general relativistic effects will become observable (see, for example, Ref. 25 or Ref. 26). Someday we may be able to observe an accretion disk around a black hole. For that case, Luminet[27] determined the optical appearance of a spherical black hole with a thin accretion disk.

The structure of this paper is as follows. In Sec. II we determine the local tetrad of a static and a freely falling observer with respect to Eddington–Finkelstein coordinates. Section III reviews some basic relations for null geodesics. In Secs. IV and V we discuss the frequency shift as well as the lensing of a star with respect to the observer's position and motion. Section VI describes the relevant details of our Qt application and provides a short manual. We end with some examples in Sec. VII.

II. LOCAL OBSERVER

The Schwarzschild spacetime is usually described in Schwarzschild coordinates $(t, r, \vartheta, \varphi)$.[3–5] However, due to the coordinate singularity at the horizon, the Schwarzschild

coordinates are not applicable for a freely falling observer crossing the horizon. Thus, we will use ingoing Eddington–Finkelstein coordinates $(v, r, \vartheta, \varphi)$. The corresponding metric is

$$ds^2 = -\left(1 - \frac{r_s}{r}\right)c^2 dv^2 + 2c\, dv\, dr + r^2 d\Omega^2, \qquad (1)$$

with the Schwarzschild radius $r_s = 2GM/c^2$ and $d\Omega^2 = d\vartheta^2 + \sin^2\vartheta\, d\varphi^2$. Here, G is Newton's constant, c is the speed of light, and M is the mass of the black hole. The relation between the Eddington–Finkelstein null coordinate v and the Schwarzschild time coordinate t is given by

$$cv = ct + r + r_s \ln\left(\frac{r}{r_s} - 1\right). \qquad (2)$$

The local reference frame of a static observer can be identified with the natural local tetrad[28]

$$\mathbf{e}_{(v)} = \frac{1}{\sqrt{1 - r_s/r}}\frac{\partial_v}{c}, \quad \mathbf{e}_{(\vartheta)} = \frac{1}{r}\partial_\vartheta, \qquad (3a)$$

$$\mathbf{e}_{(r)} = \frac{1}{\sqrt{1 - r_s/r}}\frac{\partial_v}{c} + \sqrt{1 - \frac{r_s}{r}}\partial_r, \quad \mathbf{e}_{(\varphi)} = \frac{1}{r\sin\vartheta}\partial_\varphi. \qquad (3b)$$

We call this tetrad natural because it is adapted to the symmetries of the spacetime.

To obtain the local reference frame for a freely falling observer, we use the Lagrangian formalism as described by Rindler.[3] The Euler–Lagrangian equations for a radial timelike geodesic lead to the constant of motion $k = (1 - r_s/r)c^2\dot{v} - c\dot{r}$, where a dot means differentiation with respect to the proper time τ of the falling observer. The radial motion is determined by the differential equation

$$\dot{r}^2 = \frac{k^2}{c^2} - c^2\left(1 - \frac{r_s}{r}\right), \qquad (4)$$

and the four-velocity is given by

$$\mathbf{u} = \dot{v}\partial_v + \dot{r}\partial_r = \frac{k + c\dot{r}}{c^2(1 - r_s/r)}\partial_v + \dot{r}\partial_r. \qquad (5)$$

If the freely falling observer starts from $r(\tau=0) = r_0$ with zero velocity, $\dot{r}(\tau=0) = 0$, its local reference frame is

$$\mathbf{e}_{(0)} = \frac{\sqrt{1 - r_s/r_0} - \sqrt{r_s/r - r_s/r_0}}{1 - r_s/r}\frac{\partial_v}{c} - \sqrt{\frac{r_s}{r} - \frac{r_s}{r_0}}\partial_r, \qquad (6a)$$

$$\mathbf{e}_{(1)} = \frac{\sqrt{1 - r_s/r_0} - \sqrt{r_s/r - r_s/r_0}}{1 - r_s/r}\frac{\partial_v}{c} + \sqrt{1 - \frac{r_s}{r_0}}\partial_r, \qquad (6b)$$

$$\mathbf{e}_{(2)} = \frac{1}{r}\partial_\vartheta, \quad \mathbf{e}_{(3)} = \frac{1}{r\sin\vartheta}\partial_\varphi, \qquad (6c)$$

which is regular at the horizon $r = r_s$. The corresponding magnitude of the three-velocity β with respect to a static observer with the local tetrad in Eq. (3) is

$$\beta = \sqrt{\frac{r_s/r_{\text{obs}} - r_s/r_0}{1 - r_s/r_0}}. \qquad (7)$$

With these local reference frames, we can describe the direction ξ of any incoming or outgoing null geodesic as
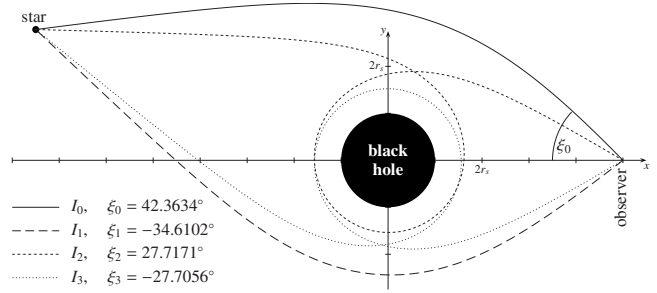

Fig. 1. A pointlike star and the observer are connected by exemplary four null geodesics I_i that have inclination angle ξ_i with respect to the local reference frame of the observer. In principle, there is an infinite number of connecting null geodesics.

$$\mathbf{y} = y^{(i)}\mathbf{e}_{(i)} = \pm\,\mathbf{e}_{(v),(0)} - \cos\xi\mathbf{e}_{(r),(1)} + \sin\xi\mathbf{e}_{(\varphi)}, \qquad (8)$$

where the sign of $\mathbf{e}_{(v)}$ or $\mathbf{e}_{(0)}$ indicates whether the four-direction points to the future $(+)$ or the past $(-)$. Because of the spherical symmetry of the spacetime, we can neglect the $\mathbf{e}_{(\vartheta)}$ direction. Note that the direction $\xi = 0$ points directly to the black hole.

III. NULL GEODESICS

Our main challenge is to find a null geodesic that connects a star to the observer, as shown in Fig. 1. Due to the strong bending of light close to the black hole, there is not a single geodesic, but an infinite number of geodesics connecting the star and the observer.

As mentioned in Sec. I, we can take advantage of the spherical symmetry of the Schwarzschild spacetime. Thus, for each star we find a plane $\mathcal{P}$ containing the observer, the star, and the complete null geodesic connecting both, as illustrated in Fig. 2.
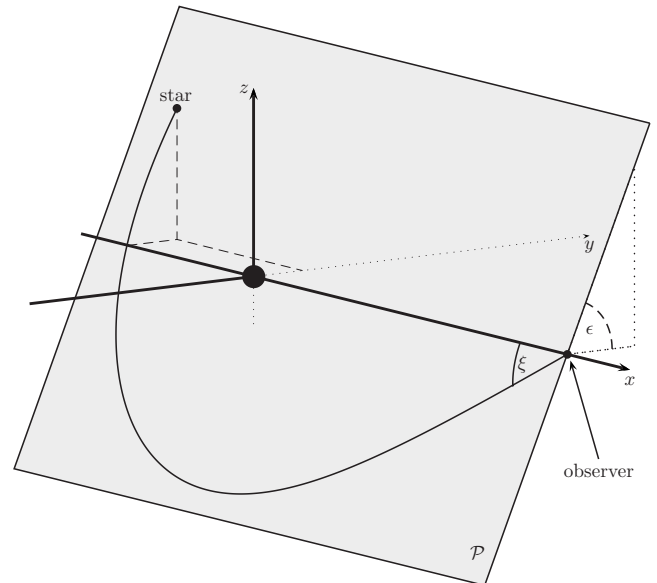

Fig. 2. Due to the spherical symmetry of the Schwarzschild spacetime, any null geodesic connecting the observer and the star rests in a plane $\mathcal{P}$ spanned by the x-axis and the star. This plane has angle ϵ to the x-y plane. The black hole is located at the origin.

The equation for the orbital motion $r = r(\varphi)$ of a null geodesic in Eddington–Finkelstein coordinates can be deduced with the Lagrangian formalism, and we obtain the same differential equation as in Schwarzschild coordinates. With the scaled coordinate $x = r_s/r$, the orbital equation reads

$$\left(\frac{dx}{d\varphi}\right)^2 = a^2 - (1-x)x^2 \tag{9}$$

with $a^2 = r_s^2/b^2 = r_s^2 k^2/(c^2 h^2)$. Here, b is the apparent impact parameter. As before, the constant of motion is $k = (1 - r_s/r)c^2 \dot{v} - c\dot{r}$, and the other constant is $h = r^2 \dot{\varphi}$. The dot means differentiation with respect to an affine parameter. Both constants can also be expressed by means of the direction ξ. From Eq. (8),

$$\frac{k}{c} = \sqrt{x - x_0}\cos \xi - \sqrt{1 - x_0} \quad \text{and} \quad h = \frac{r_s}{x}\sin \xi, \tag{10}$$

which are valid for the static observer at $x = x_0$ as well as for a freely falling one. We use only the negative sign of $\mathbf{e}_{(\nu)}$ or $\mathbf{e}_{(0)}$ because we consider incoming null geodesics.

If $x = x_0 = 2/3$ and $\xi = \pi/2$, the null geodesic follows a circular orbit. Because of the spherical symmetry of the spacetime, there is not only one circular orbit but a whole sphere of null geodesics, the photon sphere. The apparent size of the black hole is defined by the null geodesic, which, if we trace it back in time, approaches this photon sphere asymptotically. The corresponding direction ξ_{crit} of the null geodesic follows from the necessary condition $a^2 = 4/27$,

$$\cos \xi_{\text{crit}} = \frac{x_{\text{obs}}^2 \sqrt{1 - x_0}\sqrt{x_{\text{obs}} - x_0} \pm \sqrt{p(x_{\text{obs}}^3 - x_{\text{obs}}^2 + p)}}{x_{\text{obs}}^3 - x_0 x_{\text{obs}}^2 + p} \tag{11}$$

with $p = 4/27$. The positive sign is for $x \leq 2/3$, and the negative sign is for $x > 2/3$.

Equation (9) leads to an elliptic integral that can be solved analytically only by means of difficult mathematics. However, for a computer-based visualization method, it suffices to integrate Eq. (9) numerically,

$$\varphi = \int_{x_{\text{obs}}}^{x_{\text{star}}} \frac{dx}{\sqrt{a^2 - (1-x)x^2}}. \tag{12}$$

We split this integral into two branches if the null geodesic passes the point of closest approach x_{closest} to the black hole. This point follows from Eq. (9) with $dx/d\varphi = 0$,[4]

$$x_{\text{closest}} = \frac{\sqrt{3}a}{2} \left/ \cos\left[\frac{1}{3}\arccos\left(-\frac{3\sqrt{3}a}{2}\right)\right].\right. \tag{13}$$

In the following, we will trace null geodesics back in time. We will discuss null geodesics which *start* from the observer with *initial* angle ξ even though the physical reality is reverse. This ray tracing method is a common method in computer visualization.

We can simplify the calculations by neglecting the true distances to the stars. Because we restrict the observer to the close neighborhood of the black hole, we can put the stars at infinity, $x_{\text{star}} = 0$. Then, the virtual position of a star is sufficiently described by the plane angle ϵ (see Fig. 2) and the azimuthal angle $\varphi = \varphi_\infty$ (see also the discussion in Sec. VI B).

IV. FREQUENCY SHIFT

Consider a star, a scaled distance x_{star} from the black hole, which emits a light ray of frequency ν_{star}. A static observer located at x_{obs} will receive this light ray with the gravitationally shifted frequency ν_{obs} given by[4]

$$1 + z_{\text{grav}} = \frac{\nu_{\text{star}}}{\nu_{\text{obs}}} = \sqrt{\frac{1 - x_{\text{obs}}}{1 - x_{\text{star}}}}. \tag{14}$$

If the observer is in free fall, we also take the Doppler effect into account, which results in another frequency shift, $1 + z_{\text{Doppler}} = \gamma(1 - \beta \cos \xi)$, with β from Eq. (7). The total frequency shift follows from $1 + z_{\text{total}} = (1 + z_{\text{grav}})(1 + z_{\text{Doppler}})$,

$$1 + z_{\text{total}} = \frac{\sqrt{1 - x_0} - \cos \xi \sqrt{x_{\text{obs}} - x_0}}{\sqrt{1 - x_{\text{star}}}}. \tag{15}$$

Because we cannot assign a velocity β as in Eq. (7) to an observer below the horizon, we must calculate the frequency shift by means of the parallel-transported null vector $\mathbf{n}$ that is given in analogy to the direction in Eq. (8). With respect to the observer's tetrad, the incoming light ray has the null vector

$$\mathbf{n} = \nu_{\text{obs}}(\mathbf{e}_{(\nu),(0)} + \cos \xi \mathbf{e}_{(r),(1)} + \sin \xi \mathbf{e}_{(\varphi)}). \tag{16}$$

The corresponding constant of motion $k/c = (1 - x_{\text{obs}})c\dot{v} - \dot{r}$ is $k/c = \nu_{\text{obs}}(\sqrt{1 - x_0} - \cos \xi \sqrt{x_{\text{obs}} - x_0})$. We also find $k/c = \nu_{\text{star}}\sqrt{1 - x_{\text{star}}}$ for the null vector at the star. We obtain Eq. (15) also for the inside region. Note that Eq. (15) cannot become negative because ξ is valid only in the region $\xi_{\text{crit}} < \xi \leq \pi$.

V. LENSING

The gravitational lensing due to the curved spacetime results in a modification of the brightness of the stars as discussed, for example, in Refs. 18–23. It turns out that the magnification factor μ for a static or a freely falling observer follows from the ratio of the solid angles $d\omega$ of the lensed and the unlensed star,

$$\mu = \frac{d\omega_{\text{lensed}}}{d\omega_{\text{unlensed}}} = \left|\frac{\sin \varphi}{\sin \xi}\frac{d\varphi}{d\xi}\right|^{-1}. \tag{17}$$

If the observer, the black hole, and the star are aligned ($\varphi_\infty = n\pi$, $n = 1, 2, \ldots$), the observer will see an Einstein ring. Then, the magnification for a pointlike object is infinite, as illustrated by the strong peaks in Fig. 3.

For both the static and freely falling observers, the magnification decreases exponentially with increasing deflection angle and azimuthal angle φ_∞, respectively. From the point of view of the static observer, stars with $|\varphi_\infty| < \pi/2$ will shrink if the observer quasistatically approaches the black hole horizon.

For a freely falling observer above the horizon, the magnification factor $\mu = \mu_{\text{fall}}$ can also be determined from the factor μ_{stat} with respect to the static observer and the magnification due to the special relativistic aberration expression,

$$\cos \xi_{\text{fall}} = \frac{\cos \xi_{\text{stat}} + \beta}{1 + \beta \cos \xi_{\text{stat}}} \tag{18}$$

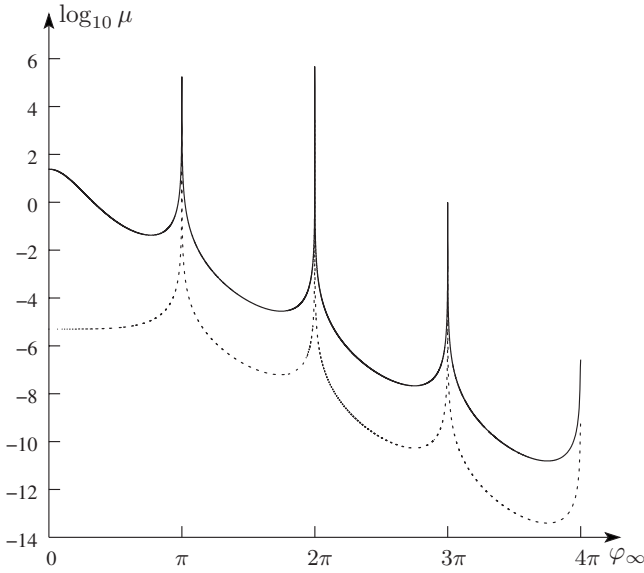with β from Eq. (7). The ratio of the solid angles of an object in special relativity is

Fig. 3. Magnification μ of a star with azimuth φ_∞ with respect to either a static observer located at $x_{\text{obs}}=0.995$ (μ_{stat}: dotted line) or a freely falling observer who started at $x_0=0$ and who is currently at $x_{\text{obs}}=0.995$ (μ_{fall}: solid line). For a star at $\varphi_\infty=n\pi$, $n=1,2,\ldots$, the observer will see an Einstein ring. Note that, in principle, the peaks are infinitely high.

$$\mu_{\text{sr}} = \frac{d\omega_{\text{fall}}}{d\omega_{\text{stat}}} = \frac{\sin\xi_{\text{fall}}}{\sin\xi_{\text{stat}}}\frac{d\xi_{\text{fall}}}{d\xi_{\text{stat}}} = \gamma^{-2}(1+\beta\cos\xi_{\text{stat}})^{-2} \quad (19a)$$

$$= \gamma^2(1-\beta\cos\xi_{\text{fall}})^2, \quad (19b)$$

where $\gamma^2=(1-\beta^2)^{-1}=(1-x_0)/(1-x_{\text{obs}})$. Then,

$$\mu_{\text{fall}} = \mu_{\text{stat}}\mu_{\text{sr}}. \quad (20)$$

Below the horizon, the magnification μ depends on the position x_0 where the freely falling observer has started. We will come back to this point in Sec. VI B.

VI. DETAILS FOR THE VISUALIZATION

The aim of our application is to interactively study the first-person view of the stellar sky in the close neighborhood of a nonrotating black hole. We use the data in the Hipparcos star catalogue containing about 118 000 stars.[30] From the Hipparcos catalogue, we obtain the right ascension α and the declination δ as well as the apparent visual magnitude m_V of each star. Because the distances of the stars to the black hole are much greater than the Schwarzschild radius, we can put the stars at infinity. The spectrum of a star is represented by a blackbody spectrum, which simplifies the computation of the frequency shift considerably. The observer can either move quasistatically around the black hole or can fall freely on a timelike, radial geodesic starting from rest at some distance r_0.

The application is written in C++ using the Qt[31] library for the graphical user interface. The visualization is done with OpenGL, for which we use the OpenGL Shading Language for the point-based star rendering.[32]

In the following, we discuss how the geometric distortion of the stellar sky and the magnification of the stars is stored within lookup tables. We also explain how the spectrum of a star is realized by a Planck spectrum and how the Fraunhofer diffraction due to a circular lens influences the visual appear-
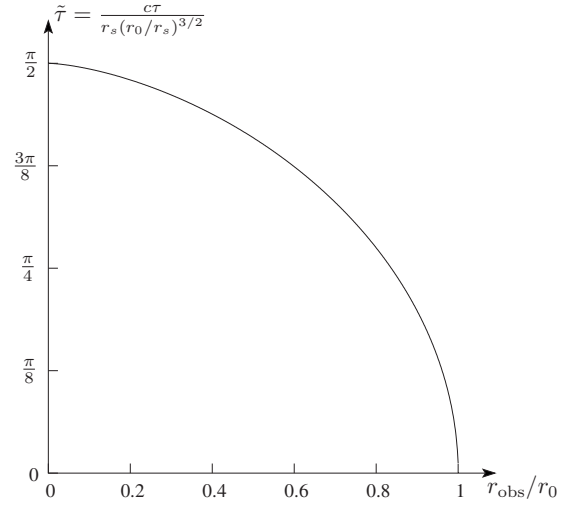

Fig. 4. Relation between the dimensionless parameter $\tilde{\tau}$ and the current position r_{obs} of a freely falling observer starting with zero velocity from $r_0>r_s$.

ance of a star. Readers who are not interested in technical details may skip Secs. VI B–VI G. These details are complementary to the emphasis on general relativity in Secs. II–V and are not needed to understand the geometric distortions.

A. Freely falling observer

For the case of a freely falling observer, we integrate Eq. (4) to obtain the relation between its proper time τ and its current position r_{obs},

$$\tilde{\tau} \equiv \frac{c\tau}{r_s(r_0/r_s)^{3/2}} = \frac{r_{\text{obs}}}{r_0}\sqrt{\frac{r_0}{r_{\text{obs}}}-1} + \arctan\sqrt{\frac{r_0}{r_{\text{obs}}}-1},$$
$$(21)$$

as shown in Fig. 4. We have introduced the dimensionless parameter $\tilde{\tau}$, which makes the right-hand side of Eq. (21) independent of the Schwarzschild radius r_s. In the limit $r_{\text{obs}} \to 0$, when the observer will crash into the singularity, Eq. (21) yields $\tilde{\tau}=\pi/2$.

Because $\tilde{\tau}$ as a function of the current position r_{obs} is a monotonic function, we can determine the inverse function $r_{\text{obs}}(\tau)$ numerically by the Brent root finding algorithm.[33]

B. Geometric distortion and magnification

Due to the strong bending of light close to a black hole, the stellar sky appears distorted. As discussed in Sec. III, we can take advantage of the spherical symmetry of the Schwarzschild metric and define a plane $\mathcal{P}$ spanned by the current position r_{obs} of the observer, the location φ_{star} of the star at infinity, and the connecting null geodesic. In this plane, a star will appear at several directions ξ_i, as seen in Fig. 1. To distinguish between the corresponding light rays, we include the order of the image into the azimuthal angle

$$\varphi_\infty = \begin{cases} \varphi_{\text{star}}+2\pi n & (n=0,2,4,\ldots) \\ 2\pi n - \varphi_{\text{star}} & (n=1,3,5,\ldots), \end{cases} \quad (22)$$

where $0\le\varphi_{\text{star}}\le\pi$.

To obtain the relation between the actual position φ_∞ of the star and the apparent position ξ for an observer located at
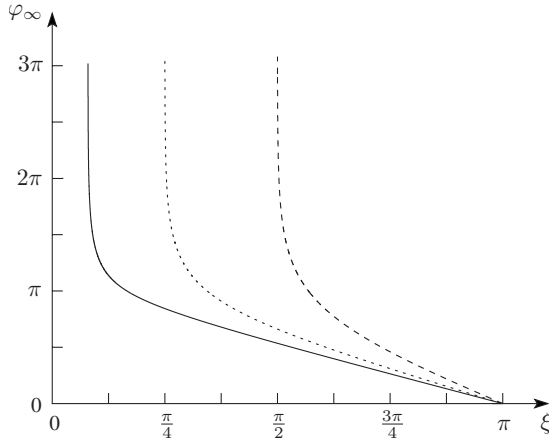
Fig. 5. A null geodesic having inclination ξ with respect to a static observer located at $x_{\mathrm{obs}} = \{\frac{1}{10}, \frac{1}{3}, \frac{2}{3}\}$ (solid, dotted, dashed lines) has an angular deviation φ_∞ due to the curved spacetime. The corresponding critical angles are $\xi_{\mathrm{crit}} = \{0.249, \pi/4, \pi/2\}$.

r_{obs}, we integrate Eq. (12) from x_{obs} to $x_{\mathrm{star}} = 0$. As an example, Fig. 5 shows the azimuthal angle φ_∞ as a function of the observation angle ξ for a static observer at three positions.

For our interactive application, we need the inverse relation ξ as a function of the current position x_{obs} and the azimuthal angle φ_∞. Therefore, we precalculate a two-dimensional (2D) lookup table, as shown in Fig. 6.

If the observer is falling freely, we adjust the apparent position ξ regarding the observer's current velocity $\beta = \sqrt{(x_{\mathrm{obs}} - x_0)/(1 - x_0)}$ using Eqs. (7) and (18).

In addition to the geometric distortion of the stellar sky, we also include the magnification as discussed in Sec. V. Hence, we expand the lookup table by the factor

$$\chi_{\mathrm{stat}} = \log_{10} \mu_{\mathrm{stat}}^{-1} = \log_{10} \left| \frac{\sin \varphi \, d\varphi}{\sin \xi \, d\xi} \right| \tag{23}$$

for a static observer.

Thus far, we only have the lookup table for the outside region $r_{\mathrm{obs}} > r_s$. Below the horizon, the observer cannot be static. In this case, we store the dimensionless parameter
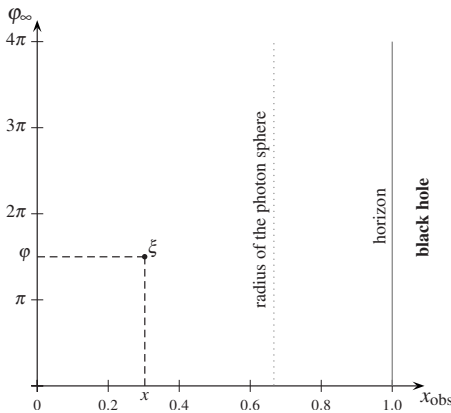

Fig. 6. The lookup table for a static observer at position $x_{\mathrm{obs}} = x$ and a star with azimuth angle φ yields the observation angle ξ. The photon sphere is located at $x = 2/3$, whereas the horizon has coordinate $x = 1$.

$$a = \frac{r_s k}{ch} = \frac{x\sqrt{x - x_0}\cos \xi - x\sqrt{1 - x_0}}{\sin \xi} \tag{24}$$

with respect to the scaled current position r_{obs}/r_s and the azimuthal angle φ_∞. Here, the constants k and h follow from Eq. (10). In the precalculation step, we can choose x_0 arbitrarily. In the application, we solve for the unknown apparent angle,

$$\xi = \arctan[Y(a, x_0, x_{\mathrm{obs}}), X(a, x_0, x_{\mathrm{obs}})], \tag{25a}$$

$$X(a, x_0, x) = x^2\sqrt{1 - x_0}\sqrt{x - x_0} + a\sqrt{a^2 - (1 - x)x^2}, \tag{25b}$$

$$Y(a, x_0, x) = x\sqrt{x - x_0}\sqrt{a^2 - (1 - x)x^2} - ax\sqrt{1 - x_0}, \tag{25c}$$

where the parameter a is read from the lookup table. A derivation of Eq. (25) is given in Appendix A. Note that the radicand in Eqs. (25b) and (25c),

$$a^2 - (1 - x)x^2 = \frac{x^2}{\sin^2 \xi}[\sqrt{x - x_0} - \sqrt{1 - x_0}\sin \xi]^2, \tag{26}$$

is always non-negative. As before, we also store the factor $\chi_\infty = \log_{10} \mu_\infty^{-1}$, where μ_∞ is calculated for an observer with initial position $x_0 = 0$. To determine the magnification μ for an arbitrary initial position x_0, we define a correction factor similar to μ_{sr} of Eq. (19a),

$$\mu_0 = \frac{d\omega}{d\omega'} = \frac{\sin \xi}{\sin \xi'}\frac{d\xi}{d\xi'}, \tag{27}$$

where $\xi' = \xi(x_0 = 0)$, as in Eq. (25a). Now, we replace a in Eq. (25a) by

$$a = \frac{x\sqrt{x}\cos \xi' - x}{\sin \xi'} \tag{28}$$

from Eq. (24), which yields a function $\xi = \xi(\xi')$ for μ_0. Hence, the magnification for an arbitrary initial position is $\mu = \mu_\infty \mu_0$.

C. Planck spectra for the stars

To simplify the visualization of the stars, we approximate the actual spectrum by a Planck spectrum. For that, we extract the Johnson B-V color of each star given in the Hipparcos catalogue and assign a temperature $T = T_{B-V}$ following the empirical law given by Reed,[34]

$$B - V$$
$$= \begin{cases} C_1 \log_{10} T + C_2 & (\log_{10} T \leq 3.961) \\ C_3(\log_{10} T)^2 + C_4 \log_{10} T + C_5 & (\log_{10} T > 3.961) \end{cases} \tag{29}$$

with $C_1 = -3.684$, $C_2 = 14.551$, $C_3 = 0.344$, $C_4 = -3.402$, and $C_5 = 8.037$. For our Sun with $(B\text{-}V)_\odot \approx 0.656$,[35] we obtain $T_\odot \approx 5900$ K.

The spectral intensity of a star with respect to the frequency ν is

$$I_{\mathrm{Planck}}(T, \nu) = \frac{2h\nu^3}{c^2}\frac{1}{e^{h\nu/(k_B T)} - 1}, \tag{30}$$

where h is Planck's constant and k_B is Boltzmann's constant.[36] Due to the relativistic Liouville theorem,[5] I_ν/ν^3 = constant, which states that the density of photons in phase
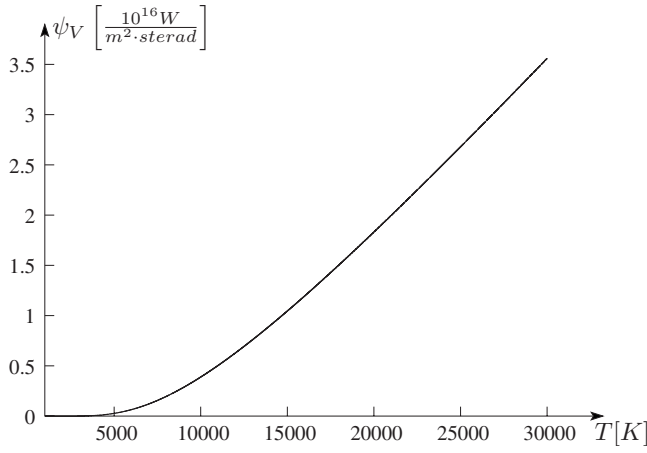
Fig. 7. The integral ψ_V of Eq. (33b) for the visual regime $V=(\lambda_1=380$ nm, $\lambda_2=780$ nm) as a function of the star temperature T.

space is constant, a frequency shifted Planck spectrum is again a Planck spectrum but with a different temperature. With the shift factor z_{total} of Eq. (15), the actual star temperature T_{star} and the temperature T_{obs} measured by the observer are related by

$$T_{\text{obs}} = \frac{T_{\text{star}}}{1 + z_{\text{total}}}. \tag{31}$$

Thus, blueshifted stars appear hotter than they are.

D. Apparent magnitude

The apparent magnitude m of a star is defined as

$$m = -2.5 \log_{10} \frac{f}{f_0}, \tag{32}$$

where f is the flux density received by the observer and f_0 is a constant scaling factor.[37] The flux density f for the wavelength domain (λ_1, λ_2) is given by the spectral intensity I_{Planck}, the solid angle $d\omega$, and the sensitivity $s(\lambda)$ of the detector,

$$f_{(\lambda_1, \lambda_2)} = d\omega \int_{\lambda_1}^{\lambda_2} I_{\text{Planck}}(T, \lambda) s(\lambda) d\lambda \tag{33a}$$

$$\equiv d\omega \, \psi_{(\lambda_1, \lambda_2)}(T). \tag{33b}$$

A brief explanation of the human sensitivity $s(\lambda) = \bar{y}(\lambda)$ is given in Appendix C. In Eq. (33b) we use the wavelength representation of the Planck spectrum, which follows from Eq. (30) together with $I_{\text{Planck}}(T, \nu) d\nu = -I_{\text{Planck}}(T, \lambda) d\lambda$ and $c = \lambda \nu$,

$$I_{\text{Planck}}(T, \lambda) = \frac{2hc^2}{\lambda^5} \frac{1}{e^{hc/(\lambda k_B T)} - 1}. \tag{34}$$

Note that we have incorporated the angular size $d\omega$ of a star only to determine the flux density f.

Figure 7 shows the integral $\psi_V = \psi_{(\lambda_1, \lambda_2)}$ for the visual regime $V = (\lambda_1 = 380$ nm, $\lambda_2 = 780$ nm) as a function of the temperature T.

From the Hipparcos catalogue, we know the apparent visual magnitude m_V of each star as well as its Reed temperature T. Hence, we can determine the factor

$$\zeta \equiv \frac{d\omega}{f_0} = \frac{10^{-0.4 m_V}}{\psi_V(T_{\text{star}})}, \tag{35}$$

which follows from Eqs. (32) and (33b).

To obtain the observed apparent visual magnitude $m_{V,\text{obs}}$, we replace $d\omega = d\omega_{\text{unlensed}}$ by the lensed expression $d\omega_{\text{lensed}} = \mu d\omega_{\text{unlensed}}$ and the integral $\psi_V(T_{\text{star}})$ by the integral $\psi_V(T_{\text{obs}})$ at the observed temperature. Thus, we obtain

$$m_{V,\text{obs}} = -2.5 \log_{10} [\mu \zeta \psi_V(T_{\text{obs}})] \tag{36}$$

or

$$m_{V,\text{obs}} - m_V = -2.5 \log_{10} \mu - 2.5 \log_{10} \frac{\psi_V(T_{\text{obs}})}{\psi_V(T_{\text{star}})}, \tag{37}$$

respectively. If $\log_{10} \mu > 0$, a star appears brighter than it really is (see Fig. 3).

E. Fraunhofer diffraction

When we observe the stellar sky with our naked eyes or through a telescope, the finite aperture a_{ap} of the iris or the lens causes Fraunhofer diffraction,[38]

$$I_{\text{Fh}}(\lambda, \eta) = I_0 \left(\frac{2J_1(k\eta)}{k\eta} \right)^2, \tag{38}$$

where I_0 is the maximum intensity, $\eta = a_{\text{ap}} \sin \theta$, θ is the observation angle within the telescope, $k = 2\pi/\lambda$ is the wave number, and λ the wavelength. J_1 is the Bessel function of the first kind (see Appendix B). The first root of Eq. (38), given by $(k\eta)_{\text{min}} \approx 3.8317$, is responsible for the resolution of the telescope. The Rayleigh criterion with $D = 2a_{\text{ap}}$ is

$$\sin \theta \geq \frac{(k\eta)_{\text{min}}}{\pi} \frac{\lambda}{D} \approx 1.2197 \frac{\lambda}{D}, \tag{39}$$

which also gives the angular size θ of the Airy disk.

The constant intensity I_0 of the Fraunhofer diffraction is replaced by the Planck spectrum of the star. But, because neither a telescope nor the human eye is sensitive to only one wavelength, we integrate the incident intensity over the domain (λ_1, λ_2),

$$I_{(\lambda_1, \lambda_2)} = \int_{\lambda_1}^{\lambda_2} I_{\text{Planck}}(T, \lambda) I_{\text{Fh}}(\lambda, \eta) d\lambda. \tag{40}$$

Figure 8 shows the integrated intensity I_V for the visual regime V. In Fig. 9 the contour plots corresponding to Fig. 8 are shown, where I_V is scaled with the maximum intensity $I_{\text{max}} = I_V(T, \eta=0)$. The gamma display correction factor is 1/4 (see Ref. 39).

F. Visualization of the stars

For the visualization of the stars, we transform the spectrum of each star onto the color space of the computer display. We first determine the color values $\Sigma_j = \{X, Y, Z\}$ in the CIE XYZ color system (Appendix C) by a convolution of the spectrum with the color matching functions $\bar{\sigma}_j(\lambda) = \{\bar{x}(\lambda), \bar{y}(\lambda), \bar{z}(\lambda)\}$,
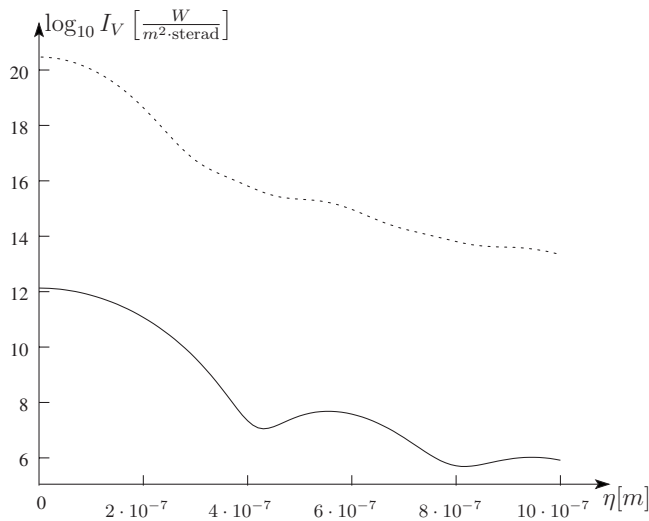
Fig. 8. Integrated intensity I_V for (a) $T=3000$ K (solid line) and (b) $T=30\,000$ K (dotted line).

$$\Sigma_{j,(\lambda_1,\lambda_2)}(T,\eta) = \int_{\lambda_1}^{\lambda_2} I_{\text{Planck}}(T,\lambda) I_{\text{Fh}}(\lambda,\eta) \bar{\sigma}_j(\lambda) d\lambda. \quad (41)$$

These color values can also be stored in a two-dimensional lookup table depending on the parameter η and the temperature T. In the application, we scale the color values by the lensed angular size $\mu d\omega$, as shown in Eq. (35).

G. Implementation details

Before running the Qt application we generate the lookup tables of Sec. VI B that are responsible for the distortion above and below the horizon. Both tables are stored as two-dimensional images (2D textures) on the GPU with a resolution of 4096×4096 texels. This image resolution yields a positional resolution $\Delta x_{\text{obs}} = 1.0/4096 \approx 0.000\,244$ and an angular resolution $\Delta \varphi_\infty = 4\pi/4096 \approx 0.003\,068$. To fill the textures, we proceed as follows. For each x_{obs}, we loop over the observational angle ξ from 0 to ξ_{crit}. The integral (12) gives the azimuthal angle φ_∞. We can write the angle ξ at texture position $[x_{\text{obs}}, \varphi_\infty]$. For the magnification factor μ, we also calculate the derivative $d\varphi/d\xi$ numerically. In addition to the distortion textures, we store the function $\psi_V(T)$ of Eq. (33b) for $\log_{10} T_{\text{min}} = 3.0$ to $\log_{10} T_{\text{max}} = 4.7$ as a one-dimensional
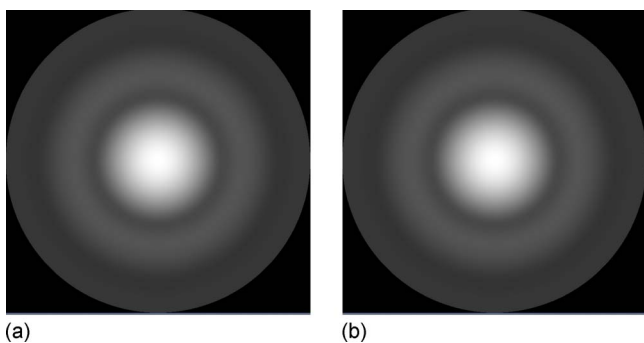

Fig. 9. Contour plot of the integrated intensity I_V/I_{max} for (a) $T=3000$ K and (b) $T=30\,000$ K.
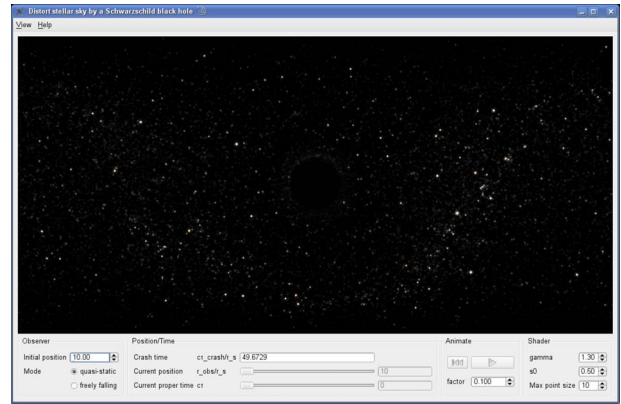
Fig. 10. Screenshot of the application with the OpenGL window (black region) and the *Observer*, *Position/Time*, *Animate*, and *Shader* panels.

texture and Σ_j of Eq. (41) as a two-dimensional texture. All lookup tables and the application code can be downloaded from Ref. 40.

The point-based rendering of the stars is done using the OpenGL Shading Language.[32] The apparent positions of the point sprites representing the stars, the frequency shift, and the magnifications are calculated by means of the vertex shader. The fragment shader is responsible for the Fraunhofer diffraction and the colors following from the apparent temperatures. A detailed discussion of the rendering pipeline and the shading language is given in Refs. 41 and 42.

H. Short description of the program

A screenshot of our Qt application is shown in Fig. 10. The main window is composed of five parts: the OpenGL window that shows the current view of the observer in 4π projection (Fig. 11) and four panels where the user can control the observer's initial position, the current position for the free fall situation, the animation of the free fall situation, and some shading parameters.

1. OpenGL window

The 4π projection shows the view of the observer in all directions. The distortion at the top and at the bottom of this projection is due to the mapping of spherical coordinates onto a plane surface and has nothing to do with the distortion due to the black hole. The advantage of this projection is that
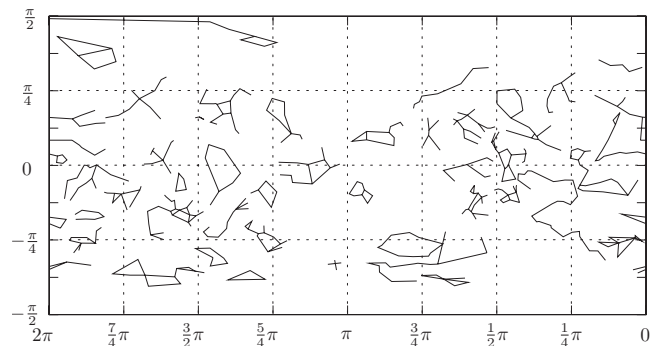

Fig. 11. 4π projection of the full sky with right ascension on the abscissa and declination on the ordinate. The constellations, taken from STELLARIUM (Ref. 14) are drawn for better orientation.
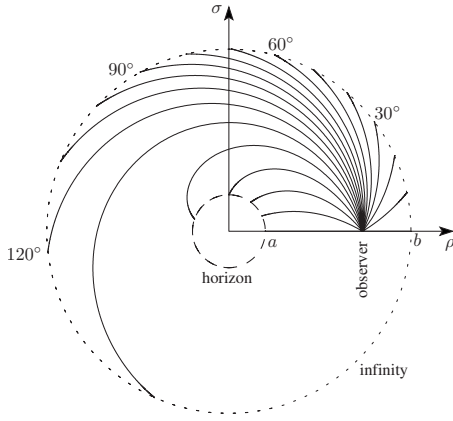
Fig. 12. Null geodesics separated by 10° with respect to the static observer located at $r_{obs}=3r_s(x_{obs}=1/6)$ will reach infinity ($x=0$) or fall into the black hole with horizon $x=1$.
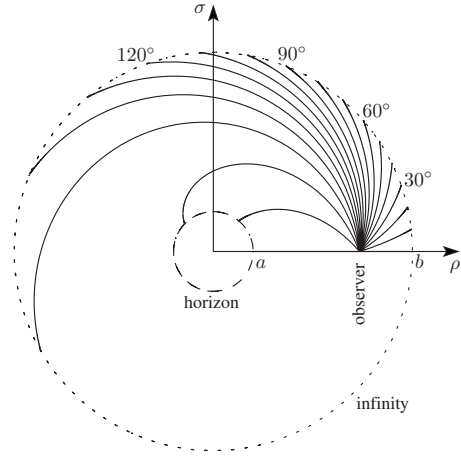

Fig. 13. Null geodesics separated by 10° with respect to the falling observer at the current position $r_{obs}=3r_s(x_{obs}=1/6)$ will reach infinity ($x=0$) or fall into the black hole with horizon $x=1$.

you can see at a glance how the complete sky will look. By pressing the left mouse button, you can quasistatically move around the black hole at a fixed radial distance with the viewing direction always pointing toward the black hole.

2. Observer panel

The initial position r_i of the observer for the free fall situation or the current radial distance for the quasistatic motion is scaled by the Schwarzschild radius r_s.

3. Position/Time panel

Depending on the initial position r_i, a freely falling observer would crash into the black hole singularity within the proper time τ_{crash}, which is scaled by the speed of light c and the Schwarzschild radius r_s. If the freely falling mode is activated, you can change either the current position or proper time of the falling observer by moving the sliders.

4. Animation

Instead of moving the sliders, you can also animate the free fall by increasing the proper time uniformly. The animate factor scales the time step.

5. Shader

The output of the star simulation is influenced by the gamma factor, f_0 of Eq. (35), and by the maximum point size which defines the size of the Airy disk.

VII. DISTORTION OF THE STELLAR SKY

To get an impression of how the bending of light distorts the stellar sky, Fig. 12 shows null geodesics for a static observer located at $x=1/6$. Here, the inner circle (horizon) has coordinate $x=1$ and the outer circle (infinity) has coordinate $x=0$. We use Cartesian coordinates (ρ, σ) with

$$\rho = [ax + b(1-x)]\cos\varphi, \tag{42a}$$

$$\sigma = [ax + b(1-x)]\sin\varphi, \tag{42b}$$

and the two scaling parameters a and b. Remember that we have neglected the actual distances of the stars and have put them at infinity.

Figure 13 shows a similar situation. The observer starts falling from infinity, $x=0$. When the observer crosses the point $x=1/6$ as shown in Fig. 12, a different distortion is observed due to the current velocity.

In addition to the geometric distortion of the stellar sky, we also take into account the gravitational frequency shift as well as the Doppler effect. Because the observer's position $x_{obs}>0$ is always closer to the black hole than the stars, the gravitational frequency shift causes the stars to appear more blue than they really are. For a static observer, Eq. (15) simplifies to $1+z_{total}=\sqrt{1-x_{obs}}$. Thus, for $x_{obs}\rightarrow1$, we have $z_{total}\rightarrow-1$. In contrast, for a freely falling observer the Doppler effect modifies the frequency shift tremendously, as seen in Fig. 14. Here, if a observer starting at $x_0=0$ crosses the horizon, the frequency shift simplifies to $z_{total}=-\cos\xi$.

Finally, let us consider the example of how light from constellation Orion is influenced by the Schwarzschild spacetime. From the Hipparcos catalogue, we obtain right ascension and declination of the single stars, as shown in Fig. 15.
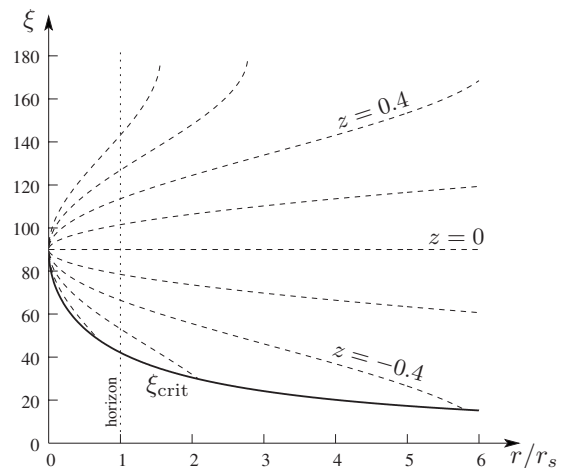

Fig. 14. For a freely falling observer starting from $x_0=0$, the black hole will appear to have apex angle $\xi=\xi_{crit}$ (solid line), as calculated from Eq. (11). The dashed lines represent lines of constant frequency shift z, as calculated from Eq. (15).
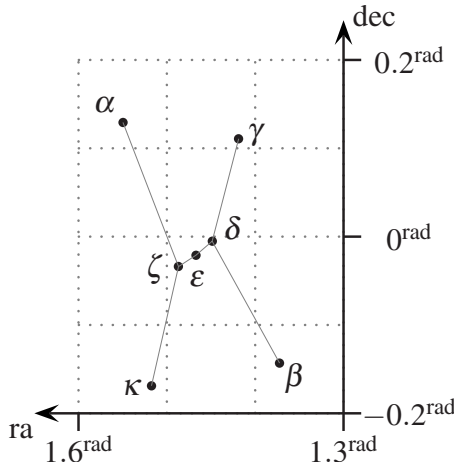
Fig. 15. Constellation Orion with coordinates given in right ascension (ra) and declination (dec). The proper names and other data are given in Table I.
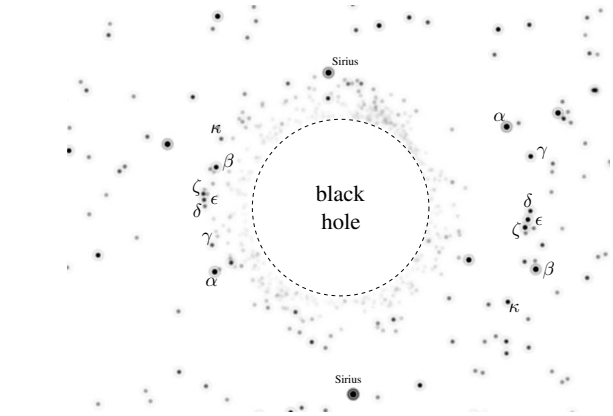

Fig. 16. Screenshot of the constellation Orion distorted by a Schwarzschild black hole. The dashed circle represents the apparent size of the black hole defined by the photon orbit $r_{ph} = 3r_s/2$. The faint rings around the stars are due to Fraunhofer diffraction.

Furthermore, we can determine a Reed temperature from the Johnson B-V color. The temperature and the apparent magnitude m_V yield the scaling factor ζ_V for the visual regime V as shown in Table I. Because ζ equals the angular size of the star divided by the scaling factor f_0, we can determine the scaled radius of each star via

$$\frac{R}{\sqrt{f_0}} \approx \sqrt{\frac{\zeta}{\pi}} d, \tag{43}$$

where d is the distance to the star. Thus, if we know the radii of the stars, we can determine the mean scaling factor f_0.

Figure 16 shows a screenshot of Orion distorted by a Schwarzschild black hole. Although the primary image of Orion looks only slightly distorted on the right side of the black hole, the mirror image of Orion on the left side looks strongly distorted. In addition, the mirror images of the stars of Orion appear fainter due to the exponential decrease in the magnification with increasing deflection angle, as discussed in Sec. V. The rings around the stars are due to the simulated Fraunhofer diffraction.

VIII. SUMMARY

The visualization of the stellar sky in the neighborhood of a Schwarzschild black hole is an excellent way of understanding the effects of general relativity. We have considered the local reference frame as well as the apparent size of the

Schwarzschild black hole for a static and a freely falling observer. The total frequency shift with respect to both observers outside the horizon is given by the product of the gravitational and the respective Doppler frequency shift. The product depends only on the initial and current position of the observer and the observation angle and can be continued beyond the horizon. In addition to the frequency shift, the change in the brightness of a star substantially depends on the change in its solid angle with respect to the observer.

The magnification for a freely falling observer outside the horizon follows from the magnification for a static observer multiplied by the magnification due to special relativistic aberration. Below the horizon, the magnification for a freely falling observer starting from an arbitrary position outside the horizon can be deduced by the magnification for a freely falling observer starting from infinity.

The distortion of the stellar sky due to the bending of light by the Schwarzschild geometry was realized by the precalculation of light rays and storing the crucial parameters in lookup tables. The numerical integration of the elliptic equation and the subsequent differentiation are numerically unstable and need more work. Currently, we use a median filter to smooth the tables.

Even though a Planck spectrum together with the empirical Reed temperature is only a rough estimate of the true

Table I. Star data of the constellation *Orion* for the stars in Fig. 15 are taken from the Hipparcos star catalogue (Ref. 30). B-V: Johnson B-V color (H37), T: temperature (Kelvins) from Eq. (29), HIP: Hipparcos number (H1), m_V: apparent visual magnitude (Johnson magnitude, H5), Trig. par.: trigonometric parallax in milli-arc-sec (H11), ζ: factor defined in Eq. (35), $R/\sqrt{f_0}[R_\odot]$: apparent radius in solar radii scaled by the constant factor f_0.

Proper name	Abbr.	B-V	T (K)	HIP	m_V	Trig.par. (milli-arc-sec)	ζ_V (m^2 sr/W)	$R/\sqrt{f_0}[R_\odot]$
Betelgeuse	α Ori	1.50	3488	27989	0.45	7.63	2.2819×10^{-14}	495
Rigel	β Ori	−0.03	9077	24436	0.18	4.22	2.8992×10^{-16}	101
Bellatrix	γ Ori	−0.22	19245	25336	1.64	13.42	1.2929×10^{-17}	7
Mintaka	δ Ori	−0.17	15279	25930	2.25	3.56	1.1586×10^{-17}	24
Alnilam	ϵ Ori	−0.18	15903	26311	1.69	1.78	1.7863×10^{-17}	59
Alnitak	ζ Ori	−0.20	17038	26727	1.74	3.99	1.4858×10^{-17}	24
Saiph	κ Ori	−0.17	14819	27366	2.07	4.52	1.4589×10^{-17}	21

spectrum of a star, it gives a realistic view for our star visualization. By means of Fraunhofer diffraction, we took the influence of a finite aperture into account.

We restricted the observer to quasistatic and radial motion. Arbitrary motion around the black hole using Fermi–Walker transport for the observer's reference frame is mathematically straightforward, but the interplay between special relativistic aberration and gravitational distortion becomes too complicated to be of pedagogical use.

We provide our visualization application as open source software so that users can learn how to implement the various aspects discussed with standard tools. Because our code uses highly efficient computer graphics techniques, an interactive exploration of the stellar sky in the vicinity of a Schwarzschild black hole is feasible.

APPENDIX A: APPARENT ANGLE

In Sec. VI B we solved an equation of the type

$$\alpha \cos \xi - \kappa \sin \xi = \beta \tag{A1}$$

with $\alpha > \beta$. To obtain the angle ξ in the full range $[-\pi, \pi]$, we replace the trigonometric functions by their complex representation, for example, $\cos \xi = \frac{1}{2}(e^{i\xi} + e^{-i\xi})$. The solution for ξ is

$$\xi = -i \ln \frac{\beta \pm \sqrt{\alpha^2 + \kappa^2 - \beta^2}}{\alpha + i\kappa} \tag{A2a}$$

$$= -i \ln \frac{x + iy}{\sqrt{x^2 + y^2}} = \arctan(y, x), \tag{A2b}$$

where

$$x = \alpha\beta \pm \kappa\sqrt{\alpha^2 + \kappa^2 - \beta^2}, \tag{A3a}$$

$$y = \pm \alpha\sqrt{\alpha^2 + \kappa^2 - \beta^2} - \beta\kappa. \tag{A3b}$$

APPENDIX B: FRAUNHOFER DIFFRACTION AND J_1

For Fraunhofer diffraction, we need the Bessel function of the first kind, which is defined as the infinite sum

$$J_n(x) = \sum_{k=0}^{\infty} \frac{(-1)^k}{k! \, \Gamma(n+k+1)} \left(\frac{x}{2}\right)^{n+2k} \tag{B1}$$

with the gamma function $\Gamma(n) = (n-1)!$ for positive integers. Fraunhofer diffraction leads to

$$\frac{I_{\text{Fh}}}{I_0} = \left(\frac{2J_1(x)}{x}\right)^2. \tag{B2}$$

The first three roots of Eq. (B2) are $x_1 \approx 3.832$, $x_2 \approx 7.016$, and $x_3 \approx 10.173$. The maxima of Eq. (B2) can be obtained
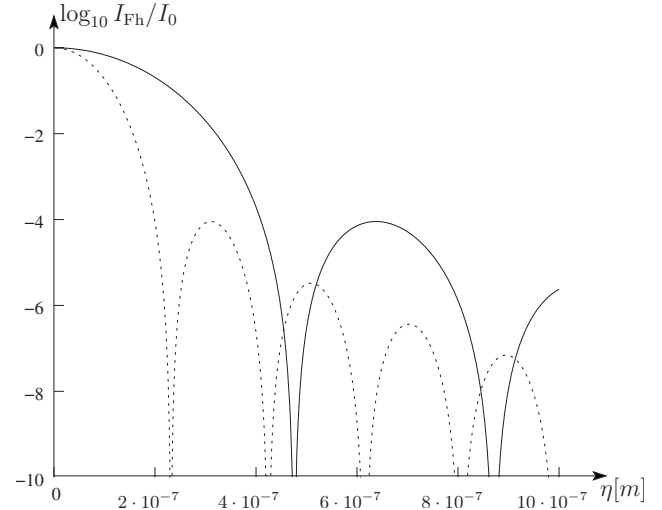
Fig. 17. Fraunhofer diffraction I_{Fh}/I_0, from Eq. (40), for $\lambda = 380$ nm (dotted line) and $\lambda = 780$ nm (solid line).

with the help of the recurrence relation $dJ_1(x)/dx = J_1(x)/x - J_2(x)$. In this way, we find the roots of $J_2(x)$, which are $\tilde{x}_1 \approx 5.136$ and $\tilde{x}_2 \approx 8.417$. Figure 17 shows the Fraunhofer diffraction depending on wavelength λ and η.

APPENDIX C: SENSITIVITY OF THE HUMAN EYE

Human visual perception is described by the tristimulus theory, which means that the color $\mathbf{C}$ is composed of three primary colors $\mathbf{X}, \mathbf{Y}, \mathbf{Z}$, where $\mathbf{C} = X\mathbf{X} + Y\mathbf{Y} + Z\mathbf{Z}$.[39] We have used the primary colors defined by the *Commission Internationale de l'Éclairage* in 1931. The coefficients X, Y, and Z follow from the spectral intensity distribution $I(\lambda)$ by convolution with the color matching functions $\bar{x}(\lambda)$, $\bar{y}(\lambda)$, and $\bar{z}(\lambda)$ (see Fig. 18).

For an arbitrary scaling factor κ, we obtain, for example,

$$Y = \kappa \int I(\lambda)\bar{y}(\lambda)d\lambda. \tag{C1}$$

The primaries are chosen in such a way that the function $\bar{y}(\lambda)$ represents the sensitivity of the human eye regarding the luminance of a color.
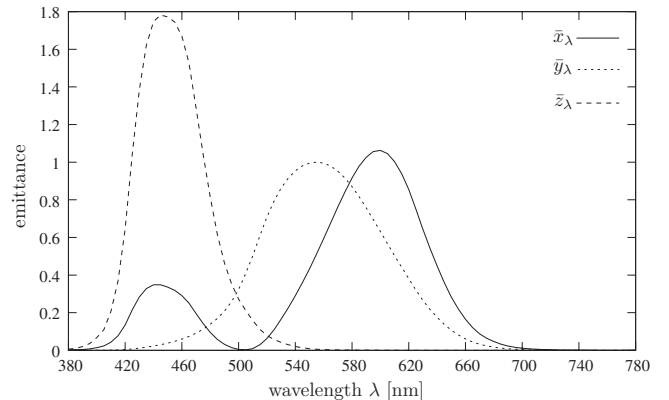
Fig. 18. CIE 1931 2 degree color matching functions $\bar{x}_\lambda, \bar{y}_\lambda, \bar{z}_\lambda$ (Ref. 43).

For a detailed discussion on the transformation between the CIE colors and the RGB values for a specific device or display, we refer the readers to Ref. 39. In our application, we use the color rendering of Ref. 44.

a)Electronic mail: thomas.mueller@vis.uni-stuttgart.de

[1] K. Schwarzschild, "On the gravitational field of a mass point according to Einstein's theory," Gen. Relativ. Gravit. **35**, 951–959 (2003), translated by S. Antoci from "Über das Gravitationsfeld eines Massenpunktes nach der Einsteinschen Theorie," Sitzungsber. K. Preuss. Akad. Wiss. **1916**,I. S.189–196.

[2] A. Einstein, "Zur allgemeinen Relativitätstheorie," Sitzungsber. K. Preuss. Akad. Wiss. **1915**,II. S.778–786.

[3] W. Rindler, *Relativity: Special, General and Cosmology* (Oxford U. P., Oxford, 2001).

[4] R. M. Wald, *General Relativity* (The U. of Chicago Press, Chicago, 1984).

[5] C. W. Misner, K. S. Thorne, and J. A. Wheeler, *Gravitation* (Freeman, New York, 1973).

[6] D. Weiskopf, "Visualization of four-dimensional spacetimes," Ph.D. thesis, Eberhard-Karls-Universität Tübingen, 2001 ⟨tobias-lib.ub.uni-tuebingen.de/volltexte/2001/240/⟩.

[7] T. Müller, "Visual appearance of a Morris-Thorne-wormhole," Am. J. Phys. **72**, 1045–1050 (2004).

[8] A. Čadež and U. Kostić, "Optics in the Schwarzschild spacetime," Phys. Rev. D **72**, 104024-1–10 (2005).

[9] T. Müller, "Exact geometric optics in a Morris-Thorne wormhole spacetime," Phys. Rev. D **77**, 044043-1–11 (2008).

[10] C. T. Cunningham, "Optical appearance of distant objects to observers near and inside a Schwarzschild black hole," Phys. Rev. D **12**, 323–328 (1975).

[11] J. Schastok, M. Soffel, H. Ruder, and M. Schneider, "Stellar sky as seen from the vicinity of a black hole," Am. J. Phys. **55**, 336–341 (1987).

[12] R. J. Nemiroff, "Visual distortions near a neutron star and a black hole," Am. J. Phys. **61**, 619–632 (1993); ⟨www.phy.mtu.edu/bht/rjn-bht.html⟩.

[13] T. Müller, "Falling into a Schwarzschild black hole—Geometric aspects," Gen. Relativ. Gravit. **40**, 2185–2199 (2008).

[14] The open source planetarium software STELLARIUM can be downloaded from ⟨www.stellarium.org/⟩.

[15] The space simulation software CELESTIA can be downloaded from ⟨www.shatters.net/celestia/⟩.

[16] The JAVA application by Slavo Tuleja can be downloaded from ⟨www.eftaylor.com/grsoftware/⟩.

[17] T. Müller and F. Grave, "GeodesicViewer—A tool for exploring geodesics in the theory of relativity," Comput. Phys. Comm. doi:10.1016/j.cpc.2009.10.010 (to be published).

[18] P. Schneider, J. Ehlers, and E. E. Falco, *Gravitational Lenses* (Springer-Verlag, New York, 1992).

[19] H. C. Ohanian, "The black hole as a gravitational 'lens'," Am. J. Phys. **55**, 428–432 (1987).

[20] J. Wambsganss, "Gravitational lensing in astronomy," Living Rev. Relativ. **1**, 12 (1998); ⟨www.livingreviews.org/lrr-1998-12⟩.

[21] K. S. Virbhadra and G. F. R. Ellis, "Schwarzschild black hole lensing," Phys. Rev. D **62**, 084003-1–8 (2000).

[22] V. Perlick, "Gravitational lensing from a spacetime perspective," Living Rev. Relativ. **7**, 9 (2004); ⟨www.livingreviews.org/lrr-2004-9⟩.

[23] S. Frittelli, T. P. Kling, and E. T. Newman, "Spacetime perspective of Schwarzschild lensing," Phys. Rev. D **61**, 064021-1–14 (2000).

[24] V. Bozza and G. Scarpetta, "Strong deflection limit of black hole gravitational lensing with arbitrary source distances," Phys. Rev. D **76**, 083008-1–20 (2007).

[25] A. E. Broderick and A. Loeb, "Imaging bright-spots in the accretion flow near the black hole horizon of Sgr A*," Mon. Not. R. Astron. Soc. **363**, 353–362 (2005).

[26] N. Hamaus *et al.*, "Prospects for testing the nature of Sgr A*'s NIR flares on the basis of current VLT- and future VLTI-observations," Astrophys. J. **692**, 902–916 (2009).

[27] J.-P. Luminet, "Image of a spherical black hole with thin accretion disk," Astron. Astrophys. **75**, 228–235 (1979).

[28] We use the differential geometric notation, where $\partial_\mu = \partial / \partial x^\mu$ is the coordinate base vector along x^μ. For a detailed discussion of this topic, see, for example, Ref. 29.

[29] M. Nakahara, *Geometry, Topology and Physics* (IOP, Bristol, 1990).

[30] The Hipparcos star catalogue consists of about 118 000 stars most of which are at a distance of roughly 100 pc. The data we are interested in are right ascension (H3), declination (H4), magnitude in Johnson V (H5), trigonometric parallax (H11), Johnson B-V color (H37), and Henry Draper (HD) catalogue number (H71). The digital catalogue I/239 can be found on ⟨cdsarc.u-strasbg.fr/viz-bin/Cat?I/239⟩ 1997HIP…C……0E—European Space Agency SP-1200 (1997).

[31] The Qt library can be found at ⟨qt.nokia.com/⟩.

[32] Information about OpenGL and the OpenGL Shading Language can be found at ⟨www.opengl.org/⟩.

[33] R. P. Brent, "An algorithm with guaranteed convergence for finding a zero of a function," Comput. J. **14**, 422–425 (1971).

[34] B. C. Reed, "The composite observational-theoretical HR diagram," J. R. Astron. Soc. Can. **92**, 36–37 (1998).

[35] D. F. Gray, "The inferred color index of the Sun," Publ. Astron. Soc. Pac. **104**, 1035–1038 (1992).

[36] The physical constants are from ⟨physics.nist.gov/cuu/Constants⟩.

[37] *Fundamental Astronomy*, edited by H. Karttunen, P. Kröger, H. Oja, M. Poutanen, and K. J. Donner (Springer-Verlag, Heidelberg, 2003).

[38] E. Hecht and A. Zajac, *Optics* (Addison-Wesley Longman, Amsterdam, 2003).

[39] J. D. Foley, A. Van Dam, S. K. Feiner, and J. F. Hughes, *Computer Graphics: Principles and Practice* (Addison-Wesley Longman, Amsterdam, 1991).

[40] See supplementary material at E-AJPIAS-78-008001 for the software and all the lookup tables.

[41] D. Shreiner, M. Woo, J. Neider, and T. Davis, *OpenGL Programming Guide* (Addison-Wesley, Boston, 2006).

[42] R. J. Rost, *OpenGL—Shading Language* (Addison-Wesley, Boston, 2004).

[43] The color matching functions can be found at the Institute of Ophthalmology, University College London ⟨cvrl.ioo.ucl.ac.uk/basicindex.htm⟩.

[44] Color rendering of spectra by John Walker ⟨www.fourmilab.ch/documents/specrend/⟩.